

Tensile properties of 3D projected 4-polytopes: a new class of mechanical metamaterial

Gabrielis Cerniauskas^a, Parvez Alam^{a,*}

^a*School of Engineering, The University of Edinburgh, Edinburgh, UK*

Abstract

In this paper, we explore the mechanical behavior of a new class of mechanical metamaterials based on the 3D projections of 4-dimensional geometries (4-polytopes) subjected to loading in tension. We demonstrate that the specific properties of mechanical metamaterials can be enhanced by more than 4-fold when optimized within a framework powered by an evolutionary algorithm. Optimized metamaterial structures were manufactured using the low-force-stereolithography prototyping technique and mechanically tested in tension. The experimental results show that the best-performing metamaterial structure, the 8-cell (tesseract), has specific yield strength and specific stiffness values in a similar range to those of hexagonal honeycombs tested out-of-plane. Nevertheless, the 8-cell structures are also cubically symmetrical and have the same mechanical properties in three orthogonal axes. The effect of structure is quantified by comparing the tensile strength against the Young's modulus of bulk solid material. We find that the final value of the 8-cell structures exceeds that of the hexagonal honeycomb by 76%. The 5-cell (pentatope) and 16-cell (orthoplex) metamaterials are shown to be more effective in bearing tensile loads than the gyroid structures, while the 24-cell (octaplex) structures exhibit the lowest ratio and possess the least optimal structure-properties relationships. The findings presented in this paper showcase the importance of macro-scale architecture and highlight the potential of 3D projections of 4-polytopes as the basis for a new class of mechanical metamaterials.

Keywords: Machine learning, Genetic algorithm, Mechanical metamaterials, High stiffness and strength, Additive manufacturing, Parametric optimization

1. Introduction

Recent developments in digital manufacturing have enabled considerable advancements in the research and development of mechanical metamaterials [1, 2, 3], structures that are judiciously designed to possess unique properties and behaviours. Due to the often complex geometries of metamaterials, digital design is typically coupled to additive manufacturing [4, 5]. The final structures typically fit into unique classes of mechanical metamaterial, which include but are not limited to: auxetic [6, 7, 5], energy-absorbing [8, 4], origami/kirigami shape-morphing [9, 10, 11] and high stiffness and strength [12, 13, 14] structures. While most mechanical metamaterials are tested in compression [13, 15, 14], some studies also consider mixed mode compressive-tensile loading on structures designed to exhibit discontinuous Poisson's ratio [16, 17], variable elasticity [18, 19] and tunable stiffness [9]. There are fewer instances where mechanical metamaterials are researched in tension than in compression. Amongst these, are included: snapping metamaterials [20], controlled snapping structures for energy absorption applications [4] and multi-stable snapping metamaterials [21], re-entrant structures with customized deformation behaviour [22], shape transforming metamaterials [23] and high-stretch structures [24]. When conceptually designing metamaterial structures, emphasis is often placed on combining different computational approaches. These are commonly structural optimization models, which are coupled with finite element simulations (FEA) [25, 23, 8, 13]. Advanced optimized methods use meta-heuristic methods and machine learning algorithms, to aid the exploration of the metamaterial design space by

*Corresponding author

Email addresses: g.cerniauskas@ed.ac.uk (Gabrielis Cerniauskas), parvez.alam@ed.ac.uk (Parvez Alam)

either carrying out parametric optimization [26, 27] of the metamaterial structures, or by enabling the exploration of inverse design approaches [7, 26]. Such approaches include evolutionary algorithms [28, 29], as well as Bayesian optimization [15, 27], gradient-descent [30, 31, 32] and neural-network-powered techniques [33, 7, 26].

Following from our previous work [34], this paper focuses on 3D projected 4-dimensional polytopes (4-polytopes) that have inherently similar fractal substructures with superior mechanical properties [35, 36, 37, 38]. 3D projected 4-polytopes have geometrical features which are self-repeating and hierarchical, and therefore show great potential in applications where high stiffness and lightweights are required [38, 39, 35]. While our previous work [34] considered the effects of compression on parametrically optimized 3D projected 4D polytopes, this paper will apply an optimization framework powered by a single objective evolutionary algorithm to enhance their specific tensile stiffnesses. In addition, we discuss how maximising the specific tensile stiffness affects other mechanical properties of these metamaterials. We apply Schlegel perspectives to project 5-cell (pentatope), 8-cell (tesseract), 16-cell (orthoplex) and 24-cell (octaplex) 4-polytopes into 3-dimensions, thereby enabling their utility as base metamaterial structures for optimization.

2. Results and Discussion

2.1. Simulation results

3D-projected 4-polytope geometries were developed using the simulation-based approach described in detail in Section 5.2. 3D projections of 5-cell, 8-cell, 16-cell and 24-cell 4-polytopes were designed with the aim of maximizing specific stiffness. An optimization framework was used to automate exploration of the design space, which monitored incremental improvements in specific stiffness with each new structure generated. Figure 1 illustrates the improvements in specific stiffness at 0% (no optimization), 25% of optimal, 50% of optimal, and 100% (full optimization) of each 3D projected 4-polytope in tension. The maximum improvement in specific stiffness through our optimization framework are 121.79%, 72.45%, 163.44% and 468.71% for 5-cell, 8-cell, 16-cell and 24-cell metamaterials, respectively. The 8-cell metamaterial structure has a specific stiffness that at 0% optimization, is greater than the fully optimized 5-cell, 16-cell and 24-cell structures. It has therefore, a base cellular architecture that is already notably higher-performance when compared against the other 3D projected 4-polytopes researched here. It also exhibits the lowest percentage increase from its unoptimized to its fully optimized states, while the 5-cell, 16-cell and 24-cell, as a percentage improvement from a base structure, can be seen to benefit significantly more through the optimization framework, clarifying that adjustments of parametric design variables can yield a wide range of metamaterial architectures with improved properties of specific stiffness.

Figure 2 shows the elastic strain energy density for each of the 3D projected 4-polytope metamaterials at different levels of optimization starting at unoptimized (0%) to fully optimized (100%). These plots show that strain energy density becomes more evenly distributed within each metamaterial structure as a function of increased levels of structural optimization. As such, each unit cell type (5, 8, 16 and 24-cell) can be seen to develop a higher overall capacity to store elastic strain energy when loaded in tension, as a function of increased level of structural optimization. Since the capacity to store strain energy is also related to the overall tensile modulus of each structure, the unit cells with the most evenly distributed strain energy densities gain the highest stiffness. The plots furthermore enable the identification of regions within each metamaterial unit cell that contribute the most towards strain energy absorption and thus the overall stiffness. Nevertheless, our broader objectives were not only to optimize the structure for stiffness, but also for lightweights. This was achieved using an coupled objective for mass minimization (cf. Section 5.2). When the apparent density is thence taken into account, we note that the fully-optimized structures for each of the 3D projected 4-polytope types, have the highest specific stiffness values as previously shown in Figure 1. Visually, the most effective strain energy density distribution is in the fully-optimized 8-cell structure, followed by the 5-cell and 16-cell structures. The structure with the most localised strain energy density, namely 24-cell, has the lowest capacity for storing strain energy and hence the lowest specific stiffness. This is due to the fact that the high strain energy density levels concentrated in a single location tend to cause early local failures within the structure under tensile loading, lowering therefore, the limit of elastic proportionality in these structures. As such, we note that the optimal structures for are the ones that are able to share strain energy most effectively throughout the larger volume of a unit cell. This can therefore be seen as a fundamental design consideration in high stiffness mechanical metamaterials. In the case of our 3D projected 4-polytopes, this can in turn, be directly correlated to the geometrical complexity of each

of the structures. The best-performing 8-cell metamaterial has the lowest levels of geometrical complexity, followed by the 5-cell and 16-cell, whereas the 24-cell, which is the least optimal in terms of performance within the range of linear elasticity, is geometrically most complex. Structures with a higher level of geometrical complexity tend to have higher numbers of sharp features, such as corners and slender edges, and this results more points within the structure where with high localized strain energies.

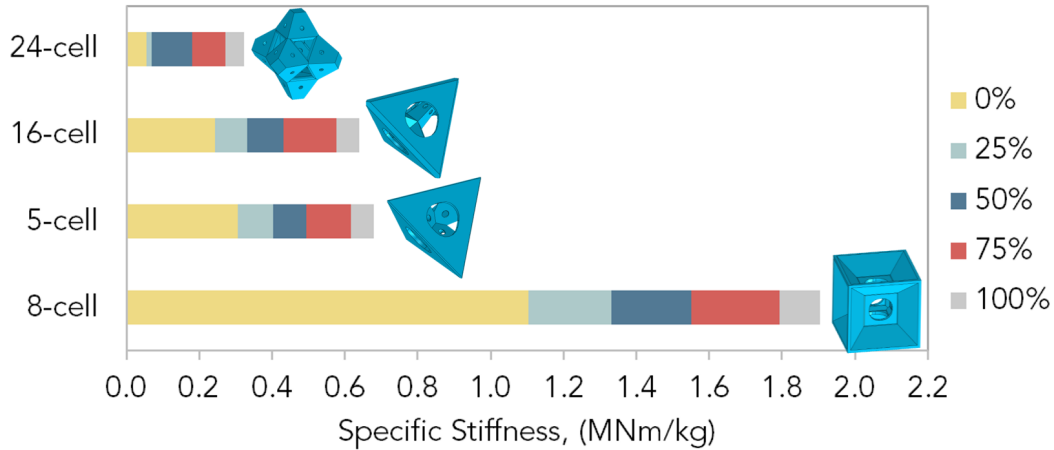


Figure 1: Specific stiffness comparisons between the 5, 8, 16 and 24-cell 3D projected 4-polytopes from unoptimized (0%) to fully optimized (100%) showing 25% increments of progression in the optimization process.

2.2. Experimental results

Figure 3 provides experimental values of specific stiffness plotted against the specific yield strength for each of the fully optimized 3D projected 4-polytope metamaterials. Also included in the figure, are experimental values for gyroids and for hexagonal honeycomb structures tested out-of-plane. The data points represent the arithmetic mean value of five experimental samples tested in tension with vertical and horizontal error bars showing the full ranges of experimental values for specific stiffness and specific yield strength, respectively. All of the samples were manufactured using the same 3D prototyping technique as discussed in Section 5.3. The experimental results follow a similar trend to the predicted simulation results, with the 8-cell metamaterial exhibiting the highest specific stiffness (0.89 MNm/kg) out of the 3D projected 4-polytope metamaterials, followed by the 5, 16 and 24-cell structures, the arithmetic means of which were 0.46, 0.40 and 0.39 MNm/kg, respectively. This is in-line with the predictions made from the simulation results where the cells with highly distributed strain energy density were found to have a higher capacity for storing strain energy and hence an overall higher stiffness. Specific yield strength values for the 3D projected 4-polytope metamaterials follow a slightly different trend, with the 8-cell structure still exhibiting the highest value of specific strength (6.71 kNm/kg), but this is then followed by the 5-cell, 24-cell and then 16-cell structures, the arithmetic means of which were 4.60, 4.48 and 3.13 kNm/kg, respectively. The higher specific strength of the 24-cell metamaterial as compared to the 16-cell structure, is presumably a result of the central alignment of the 24-cell metamaterial unit cells enabling a higher level of elastic energy absorption prior to failure and suggesting that the unique geometrical features in individual unit cells of these metamaterials play an important role in determining the load bearing to the point of yield. Moreover, as shown by the simulation results summarized in Figure 2, the elastic strain energy density is more localized in the 16-cell structure than it is in the 24-cell structure. In addition, it can be observed that all 3D projected 4-polytope metamaterials have higher specific stiffness and strength values than the gyroid structure. When compared to the hexagonal honeycomb loaded in the out-of-plane direction, we note that the arithmetic means for each 3D projected 4-polytope metamaterial type is lower in terms of specific stiffness, and that only the upper experimental range of the 8-cell structure overlaps with the arithmetic mean value of the honeycomb. Nevertheless, the 8-cell structure has the highest specific yield strength when compared to any of the six structures presented here, including that of the hexagonal honeycomb. Here, the mean value is 1.05% higher than

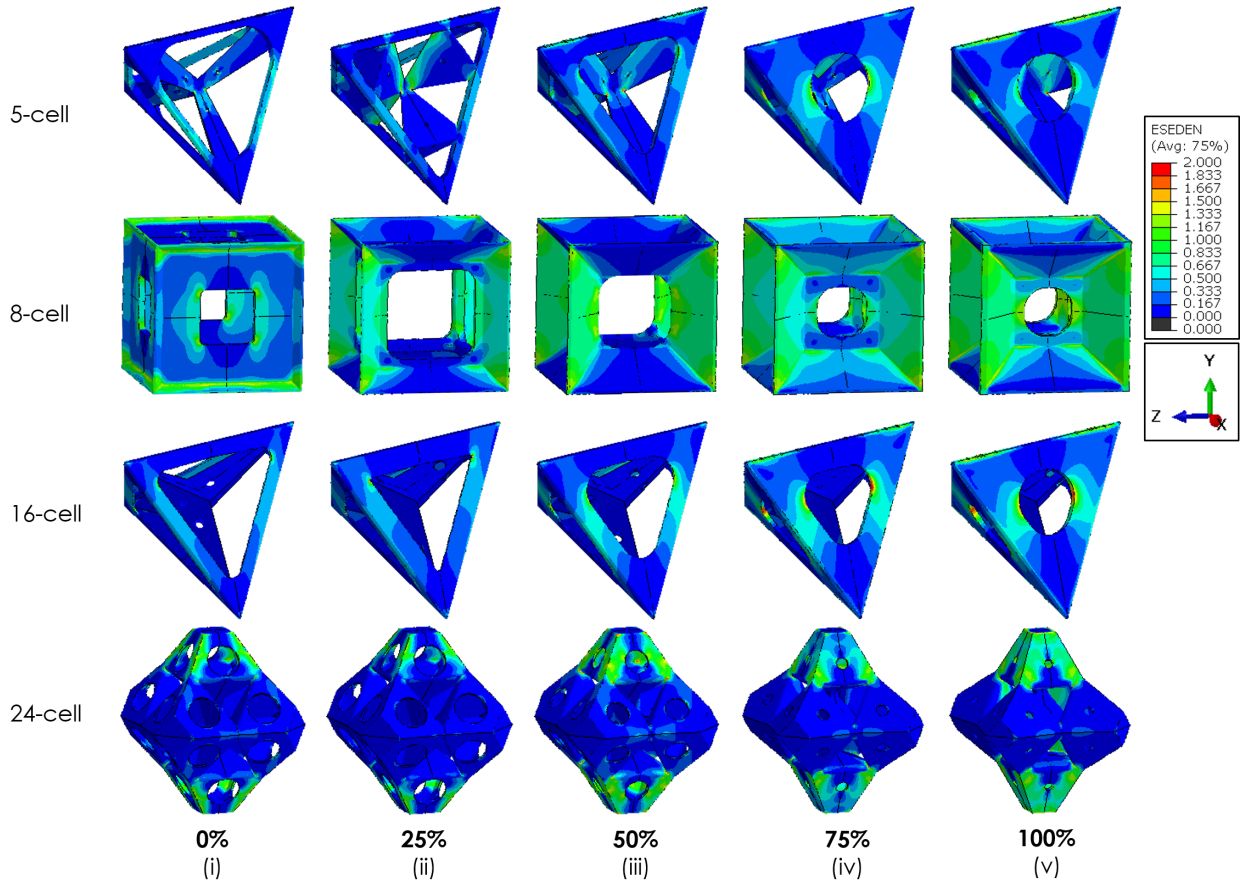


Figure 2: Color maps for each of the 3D projected 4-polytope metamaterials. Each column illustrates the progress in optimization at the following different stages: (i) 0% (unoptimized), (ii) 25%, (iii) 50%, (iv) 75% and (v) 100% (fully optimized). The color legend represents the elastic strain energy density (ESEDEN) values in J/cm^3 and the cells are loaded in tension to 4% strain.

that of the honeycomb. Similarly to the hexagonal honeycomb, the 8-cell has thin-walled features aligned along the direction of loading and hence such an arrangement contributes towards the high specific stiffness and high specific yield strength values. Moreover, the 8-cell structure was developed using an optimisation approach which implicitly reduces stress concentration points by adjusting geometrical features within the unit cell. The 8-cell structure unlike the honeycomb, has cubic symmetry (i.e. identical mechanical properties in three orthogonal axes). The honeycomb structure in comparison, is essentially a 2-dimensional structure that is extruded in the 3rd dimension, and which has high stiffness and strength in only the out-of-plane direction.

The experimental specific stiffness and specific yield strength results discussed in the preceding paragraph are also summarized in Tables 1 and 2, respectively. The tables provide the arithmetic means, experimental ranges, medians, standard deviations and coefficients of variance. Additionally, the experimental results are compared against the simulation outputs using percentage differences and Z-score (Z) values. As shown in Table 1, the simulated specific stiffness results are 3.22%, 19.16%, 19.49% and 25.75% higher than the results obtained experimentally for the 8, 24, 5 and 16-cell structures, respectively. The Z-score values follow a similar trend and are between 0.77 and 20.72, with the 8-cell having the lowest Z-score, while the 16-cell has the highest. The results summarized here indicate that the simulation predicts the specific stiffness of the 8-cell structure with a good level of accuracy. A different trend is observed when comparing specific yield strength results. The simulation output suggests significantly higher values are possible, with the percentage difference ranging between 67.06% and 77.05%, while the Z-score values are between 16.64 and 65.15. In this case, simulation results overestimate the values. This difference in simulation-predicted and

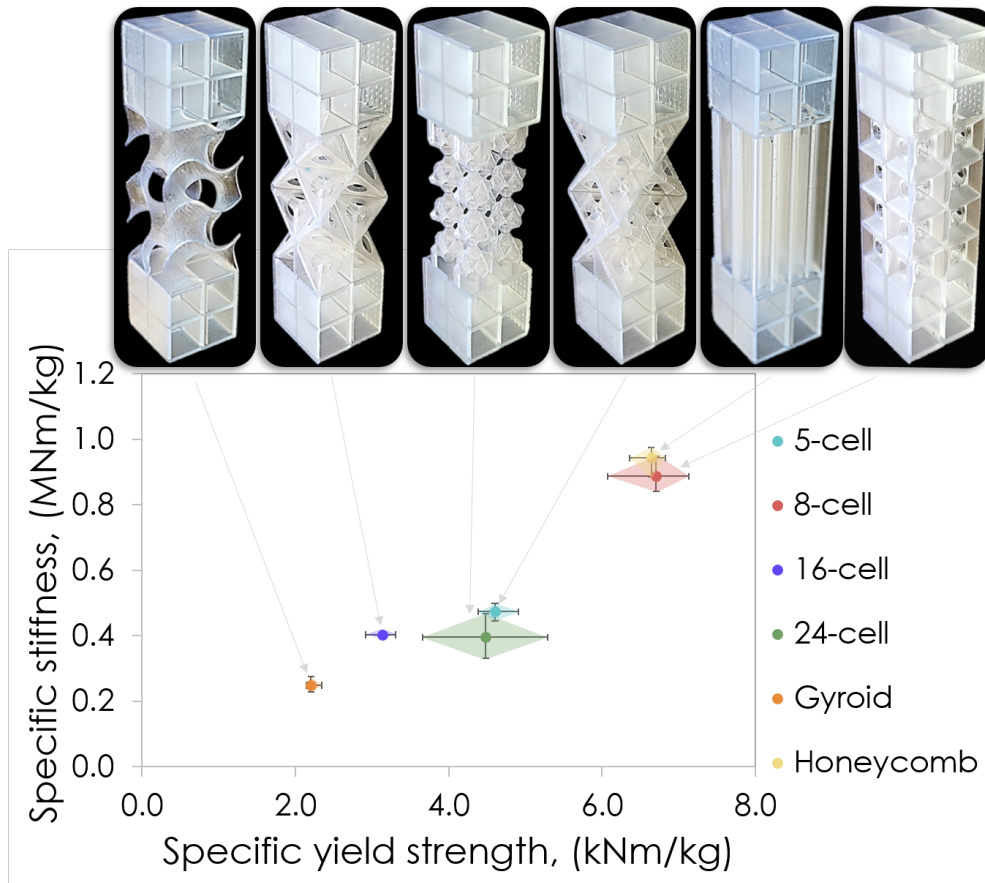


Figure 3: Specific properties plot comparing the experimental results of the 3D projected 4-polytope metamaterials with gyroid and honeycomb structures in tension.

experimentally tested behaviors can also be observed in Figure 4. Here, stress-strain curves obtained from simulations are plotted in dashed lines while the upper and lower experimental testing bounds are shown in solid lines. The simulations predict the sample stiffness with high accuracy, especially at low strain values and in each of the 3D projected 4-polytope metamaterials, the simulation results lie closer to the upper bound of the experimental results. As the tensile strain values increase, the gradients of the simulation and experimental curves start diverging indicating that the unit cell structures undergo plastic deformation at significantly lower strain values than predicted by the computational models. Consequently, the yielding strength values of the metamaterials presented here are also overpredicted by the simulation results. The main reasons for such discrepancies are due to (1) manufacturing-related limitations and (2) a low number of neighbouring unit cells in the tensile samples. As discussed in Section 5.3, the experimentally measured weights were found to be higher than that calculated from the CAD models used in the simulations by 11.62%, 0.95%, 12.67% and 11.80% for the 5, 8, 16 and 24-cell structures, respectively. Higher weight directly affects the apparent density values leading to lower overall predictions of the specific properties when compared with simulation results. The 8-cell experimental samples were only 0.95% higher in weight than the equivalent CAD models while also having the most accurate simulated specific stiffness predictions with a difference of 3.22% between simulations and experiments. The structure with the highest noticeable difference between simulated and experimentally obtained specific stiffness results (25.75%) also has the highest sample weight variation (11.80%). Higher sample weights can result from additional resin deposition within a unit cell during the manufacturing process. Any unwashed resin within the unit cell may accumulate at specific locations, such as corners and pockets. The additional resin partially cures during the post-curing process. This unwanted material may cause asymmetrical deformation of a structure under loading, giving rise to stress concentrations and leading to premature yielding. This issue is further pronounced

by the variations in material properties due to uneven polymer cross-linking during post-curing. As the samples are exposed to UV light, the level of polymerization is affected by the geometry of the metamaterial structure as well as its surface-to-volume ratio. As such, polymer cross-linking levels vary between individual samples as well as between different metamaterial sample sets. This variability can be observed in Figure 4 when comparing the upper and lower bounds of the experimental results. In addition to these manufacturing-related limitations, the experimental results are affected by the low number of neighbouring unit cells in the tensile samples. The 2x2 unit cell arrangement in the cross-section of the tensile sample was chosen to ensure that the samples could be tested using the 32mm sized tensile testing grips, however, such an arrangement is far from ideal for a unit-cell-based metamaterial. In fact, simulation results by [40] suggest that the ratio of sample cross-section to unit cell size should be higher than 10 to adequately homogenize a mechanical metamaterial.

As the simulations do not account for manufacturing imperfections and have unit cell boundary conditions that are representative of an infinite-size sample, the simulation outputs compute an idealized metamaterial response. Thus, high prediction accuracy is observed for stiffness values at low strain rates while the stress levels within the structure are low, and geometrical as well as material property-related imperfections do not play a key role in the deformation of the metamaterial structure. As strain increases, the significance of the mentioned imperfections exacerbates causing the unit cell geometries to deform in an asymmetrical manner, therefore causing premature local point yielding of the structure. Consequently, this affects the observed experimental stress-strain behavior where the experimental samples tend to have a semi-linear part of the curve after the yield point which is different to the strain-softening type of behavior predicted by the simulations. Such behavior is believed to be a superposition of asymmetrical elastic deformation of the whole unit cell as well as the local point yielding within the structure due to sample imperfections.

Table 1: Mean specific stiffness ($\frac{\bar{E}}{\rho}$) results for experimental 4-polytope metamaterial samples (5, 8, 16 and 24-cell) together with gyroid and hexagonal honeycomb results. The experimental results are compared against the simulated specific stiffness ($\frac{\bar{E}}{\rho}$) outputs using percentage differences and Z-score values.

Experimental	5-cell	8-cell	16-cell	24-cell	Gyroid	Hex honeycomb
Mean specific stiffness ($\frac{\bar{E}}{\rho}$) (MNm/kg)	0.47	0.89	0.40	0.39	0.25	0.94
Upper value	0.50	0.95	0.41	0.47	0.28	0.98
Lower value	0.45	0.84	0.39	0.33	0.23	0.89
Median	0.47	0.87	0.41	0.37	0.24	0.96
Standard deviation (S)	0.019	0.038	0.007	0.053	0.020	0.033
CoV	4.12%	4.29%	1.67%	13.39%	8.18%	3.50%
<hr/>						
Simulation						
Specific stiffness ($\frac{\bar{E}}{\rho}$) (MNm/kg)	0.59	0.92	0.54	0.49	N/A	N/A
Percentage diff. (sim. vs exp.)	19.49%	3.22%	25.75%	19.16%	N/A	N/A
Z-score ($Z = \frac{\frac{\bar{E}}{\rho} - \bar{E}}{S}$)	5.88	0.77	20.72	1.77	N/A	N/A

The specific stiffness and strength results presented so far were engineered using a computational approach which aimed to maximise the total stored elastic strain energy in each of the 3D projected 4-polytope metamaterials. However, recognizing how such an approach affects other mechanical properties allows us to compare 3D projected 4-polytope metamaterials in more detail, and to better understand the mechanical performance of these structures. Table 3 summarises the Young’s modulus, yield and tensile strengths, and modulus of resilience and toughness values for each of the 3D projected 4-polytope metamaterials, as well as for the gyroid and hexagonal honeycomb structures. The standard deviation (SD) and coefficient of variance (CoV) values are also included in Table 3 for each sample.

Stress-strain plots representative of the experimental results summarized in Table 3 are shown in Figure 5 (a) to provide a better insight into the experimental results. The 8-cell structure has the highest Young’s modulus of 213.93 MPa which is 17.62% higher than that of the hexagonal honeycomb structure tested in the out-of-plane direction with the value of 181.88 MPa. The 5-cell and 16-cell structures have values of 86.99 and 60.41 MPa, respectively, surpassing the gyroid which has Young’s modulus of 27.12 MPa. The structure with the lowest value of 25.13 MPa

Table 2: Mean specific yield strength ($\frac{\sigma_y}{\rho}$) results for experimental 4-polytope metamaterial samples (5, 8, 16 and 24-cell) together with gyroid and hexagonal honeycomb results. The experimental results are compared against simulated specific yield strength ($\frac{\sigma_y}{\rho}$) outputs using percentage differences and Z-score values.

Experimental	5-cell	8-cell	16-cell	24-cell	Gyroid	Hex honeycomb
Mean specific yield strength ($\frac{\sigma_y}{\rho}$) (kNm/kg)	4.60	6.71	3.13	4.48	2.20	6.64
Upper value	4.91	7.13	3.31	5.29	2.34	6.83
Lower value	4.38	6.07	2.92	3.66	2.15	6.36
Median	4.56	6.74	3.17	4.34	2.17	6.74
Standard deviation (S)	0.202	0.354	0.161	0.588	0.072	0.192
CoV	4.39%	5.28%	5.15%	13.12%	3.29%	2.89%

Simulation	5-cell	8-cell	16-cell	24-cell	Gyroid	Hex honeycomb
Specific yield strength ($\frac{\sigma_y}{\rho}$) (kNm/kg)	13.98	28.13	13.65	14.26	N/A	N/A
Percentage diff. (sim. vs exp.)	67.06%	76.16%	77.05%	68.58%	N/A	N/A
Z-score ($Z = \frac{\sigma_y - \bar{\sigma}_y}{S}$)	46.39	60.54	65.15	16.64	N/A	N/A

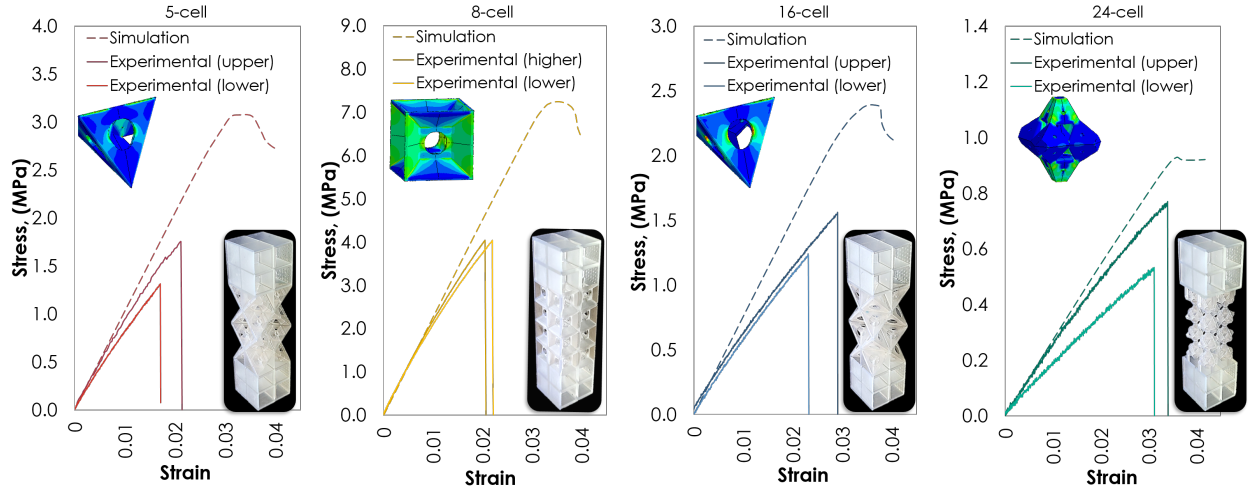


Figure 4: Stress-strain plots for 5-cell, 8-cell, 16-cell and 24-cell 4-polytope metamaterials. Simulated results are presented as dashed lines while upper and lower experimental result bounds are shown as solid lines.

is the 24-cell, however, the 24-cell also has the lowest apparent density of 63.48 kg/m^3 out of the six experimentally tested samples as presented in Table 4. The coefficient of variance values for all of the samples are between 1.67% and 13.39% showing a high level of consistency between the experimental sample results. A similar trend is observed when analyzing yield and tensile strength results. The 8-cell structure has the highest values of 1.62 and 3.67 MPa for yield and tensile strength, respectively, which are 26.56 % and 76.44% higher than those of the hexagonal honeycomb with 1.28 and 2.08 MPa for the yield and tensile strength results, respectively. Following the 8-cell and the hexagonal honeycomb, the highest yield strength values in descending order were obtained for 5-cell, 16-cell, 24-cell and gyroid structures, respectively. The tensile strength results follow a similar trend to those for yield. Following the 8-cell and hexagonal honeycomb structures, the highest tensile strength values, in descending order, were obtained for the 5-cell, 16-cell, gyroid and 24-cell structures, respectively. Although the trend is similar, it should be noted that the 24-cell structure yields at 16.67 % higher stress in comparison to the gyroid structure, however, it has a 32.99 % lower tensile strength value. These results are expected since the 3D projected 4-polytope metamaterials were designed using computational methods to maximize the elastic strain energy storage capacity, which directly correlates to the

Table 3: Summary of experimentally obtained mechanical properties for 4-polytope metamaterials as well as gyroid and hexagonal honeycomb samples. The table presents Young’s modulus, yield and tensile strength and modulus of resilience and toughness values.

	5-cell	8-cell	16-cell	24-cell	Gyroid	Hex honeycomb
Young’s modulus, (MPa)	86.99	213.93	60.41	25.13	27.12	181.88
SD	3.58	9.18	1.01	3.37	2.22	6.36
CoV	4.12%	4.29%	1.67%	13.39%	8.18%	3.50%
Yield strength, (MPa)	0.85	1.62	0.47	0.28	0.24	1.28
SD	0.04	0.09	0.02	0.04	0.01	0.04
CoV	4.39%	5.28%	5.15%	13.12%	3.29%	2.89%
Tensile strength, (MPa)	1.44	3.67	1.24	0.65	0.97	2.08
SD	0.18	1.10	0.26	0.08	0.07	0.79
CoV	12.56%	30.12%	21.33%	11.98%	7.71%	38.02%
Modulus of resilience, (kJ/m ³)	4.29	5.30	1.81	1.84	0.96	4.67
SD	0.30	0.52	0.13	0.23	0.06	0.40
CoV	7.06%	9.86%	7.10%	12.65%	6.10%	8.47%
Modulus of toughness, (kJ/m ³)	14.06	44.12	15.63	11.56	25.88	17.45
SD	3.74	20.87	7.11	1.67	9.43	14.09
CoV	26.64%	47.30%	45.49%	14.48%	36.43%	80.75%

Table 4: Apparent and relative densities for simulated and experimentally tested samples. The table includes percentage difference values between simulated and experimentally obtained apparent densities.

	Simulations		Experimental	
	Apparent density, (kg/m ³)	Relative density	Apparent density, (kg/m ³)	Relative density
5-cell	164.57	14.13%	183.70	15.77%
8-cell	238.81	20.50%	241.08	20.69%
16-cell	132.86	11.40%	149.70	12.85%
24-cell	55.78	4.79%	63.48	5.45%
Gyroid	N/A	N/A	108.82	9.34%
Honeycomb	N/A	N/A	192.89	16.56%

overall stiffness of the structure. The ability to absorb elastic strain energy can also be evaluated by comparing the modulus of resilience values for the experimental samples. The experimental results suggest that the 8-cell structure has the highest modulus followed by the hexagonal honeycomb and then the 5-cell, with values of 5.30, 4.67 and 4.29 kJ/m³, respectively. When expressed as a percentage difference with respect to the honeycomb value, the 8-cell has a 13.49% higher, while the 5-cell has an 8.14% lower modulus of resilience, suggesting that both the 8-cell and 5-cell metamaterials are highly suited for applications where elastic energy absorption is desirable. Both the 16-cell and 24-cell structures outperform the gyroid by 88.54% and 91.67%, respectively, in terms of the modulus of resilience. Lastly, as the tensile strain increases and the plastic deformation range is reached, all of the 4-polytope metamaterials fail at the tensile strain range between 0.018 and 0.034, which is higher than that of the honeycomb, which has a strain to failure value of 0.014, and lower than the gyroid, which has a strain to failure value of 0.042, as shown in Figure 5. The modulus of toughness is highest for the 8-cell with a value of 44.12 kJ/m³, which is 70.48% greater than that of the gyroid. The relatively high toughness of the 8-cell is a consequence of the high Young’s and plasticity moduli, while the gyroid has the second highest toughness due to the sample failing at high strains, rather than due to it having a high modulus. The rest of the experimental samples have toughness values that are within the range of 11.56 and 17.45 kJ/m³.

Figure 5 (b) shows the tensile strength normalized by the Young’s modulus of fully cured 3D printing resin, and is plotted against the relative density of the experimental samples summarized in Table 4. This normalization approach allows visualization of the strength gain due to the metamaterial structure, rather than its bulk material properties [41]. The structure with the highest tensile strength to modulus ratio is the 8-cell indicating that the tesseract arrangement is highly effective for applications requiring high tensile stiffness and strength, as previously shown using stiffness and

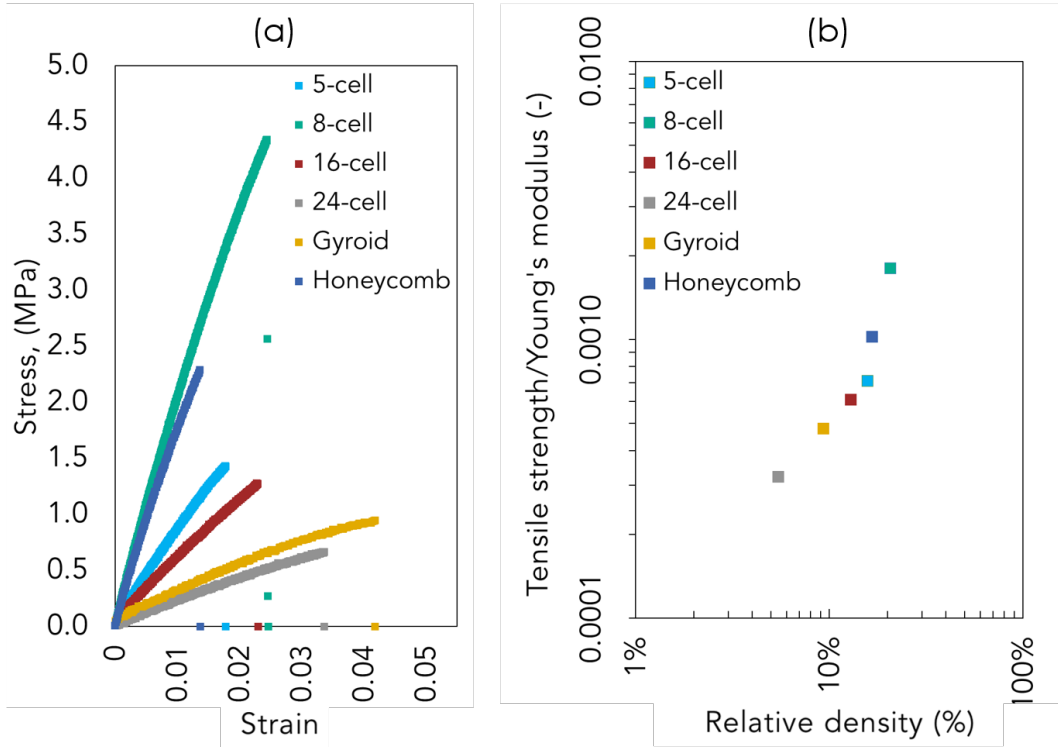


Figure 5: (a) Representative experimental tensile stress-strain curves for the 4-polytope metamaterials as well as gyroid and honeycomb samples, and (b) experimental tensile strength values normalised by material bulk Young's modulus and plotted against relative sample density.

tensile strength values (cf. Table 3). In a descending order of performance, the 8-cell is followed by the hexagonal honeycomb, the 5-cell, 16-cell and gyroid structures with the 24-cell having the lowest strength gain as a result of its architecture.

3. Conclusions

In this paper, we designed and optimized novel metamaterial structures under tension using 3D projections of 4D geometries (4-polytopes) as a basis structure. This is a new class of parametrically optimized cubically symmetrical mechanical metamaterials and we showed that they exhibit superior properties of specific stiffness and strength when compared to more conventional structures such as gyroids and honeycombs. While gyroids are also cubically symmetric, each of the four 3D projected 4-polytope metamaterials outperformed the gyroid in terms of both specific stiffness and specific yield strength. Under the optimization framework, the specific stiffness properties of the initial 4-polytope projections were improved by 122%, 72%, 163% and 469% for 5-cell (pentatope), 8-cell (tesseract), 16-cell (orthoplex) and 24-cell (octaplex) metamaterials. However, not all 4-polytope projections yielded promising final properties. In addition to the gyroid, the experimental results were also benchmarked against the well-known and commonly used hexagonal honeycomb structure tested in the out-of-plane direction. The optimised 8-cell (tesseract) structure exhibited a higher specific yield strength than the honeycomb and a marginally lower average specific stiffness. Our results demonstrate that by coupling evolutionary algorithm-based optimization methods with parametric design, we can enhance the mechanical performance of mechanical metamaterials without compromising weight. While the focus of this paper is specific stiffness and strength under tensile loading conditions, the design and optimization framework presented here can also be used to optimize for a range of other mechanical properties under different loading conditions.

4. Data Availability

All data for this paper will be made available through the Edinburgh Data Share website.

Author Contributions

Conceptualization (PA); Data curation (GC and PA); Formal analysis (GC and PA); Funding acquisition (PA); Investigation (GC); Methodology (GC and PA); Project administration (GC and PA); Resources (GC and PA); Software (GC); Supervision (PA); Validation (GC and PA); Visualization (GC and PA); Roles/Writing - original draft (GC); Writing - review and editing (PA).

5. Methodology

5.1. Design of 3D projected 4-polytope unit cell structures

The four metamaterial architectures presented in this paper were developed using regular convex 4-polytopes as baseline geometries. The specific 4-polytopes used were: 5-cell (pentatope), 8-cell (tesseract), 16-cell (orthoplex) and 24-cell (octaplex), and each is shown as a Schlegel diagrams in Figure 6 (a). The Schlegel perspective reduces these 4-polytopes from 4-dimensions to 3-dimensions and thus enables the visualization of these geometries as projections in 3-dimensional space. Each of the wireframe structures in Figure 6 (a) were then used to create a single metamaterial unit cell by using the edges and vertices of the wireframe as the contours for the thin-walled structures shown in (b) and (c), as semi-transparent and solid unit cell models, respectively. As the wireframes only present points in 3-dimensional space, rather than a solid body geometry, the thin-walled features were created to closely follow the boundaries of the projected 4-polytopes. In a similar manner to the wireframe representations, the thin-walled unit cells maintained geometrical cubic symmetry and all associated symmetry planes. This approach to metamaterial design provided flexibility such that solid features within the unit cell could be easily adjusted while following the silhouette of the projected 4-polytope structures. To exploit this flexibility, the solid features were parametrized as shown in Figure 7 and annotated in Table 5 to adjust the overall geometry of a unit cell and allow the generation of different thin-walled structures that are developed based on the same 4-polytope projections. This parameter-adjustment also enabled changing of the perspective depth while still abiding by the geometrical definition of 4-polytopes and maintaining the same symmetry planes within the unit cell. For example, the change in the perspective depth for an 8-cell unit cell enlarges or shrinks the geometrical primitive, the inner cube, within the structure. As the result, this affects the mechanical properties of the structure while also allowing the generation of an infinite number of different unit cells stemming from the same 4-polytope. Additionally, to ensure the manufacturability of the designs using a low force stereolithography (LFS) method, drain holes were introduced to allow the resin to circulate within the structure as shown in Figure 7. The external dimensions of the unit cells were constrained by a bounding box of a cubical shape with an edge length of 15 mm and these were kept the same for each of the generated designs. This ensured that only the internal geometry of a 3D projected 4-polytope structure can be altered, while the boundary conditions are kept constant. As such, regardless of the geometrical variations through optimization, unit cells could still be stacked together in a linear manner to form a metamaterial consisting of unit cell arrays.

5.2. Set up for simulations and parametric optimization

Computational unit cell models were developed for each of the 3D projected 4-polytope structures using a commercially available finite element analysis package (Abaqus/Implicit by Dassault Systèmes) to determine the elastoplastic mechanical behavior and properties of the structures under tension. The material properties used in the models are representative of the coupon samples manufactured using Formlabs Clear V4 fully-cured resin and tested in tension with Young's modulus value of 2.03 GPa, Poisson's ratio of 0.38 and density of 1.164 g/cm³. A yield strength, σ_y , of 70.32 MPa is reached under loading and the material experiences a strain-softening phase, which is defined as $\sigma_y = 44.99 \times \epsilon_y^{-0.142}$, where ϵ_y is yield strain. As all of 3D projected 4-polytopes analyzed in this paper have cubic symmetry, only one quarter of each unit cell was modelled in order to make the simulations more efficient and to reduce the computational time. To achieve that, symmetry boundary conditions were prescribed to the inner X (orange dashed line) and inner Z (red dashed line) planes as shown in Figure 8. To simulate tensile loading, the bottom of each

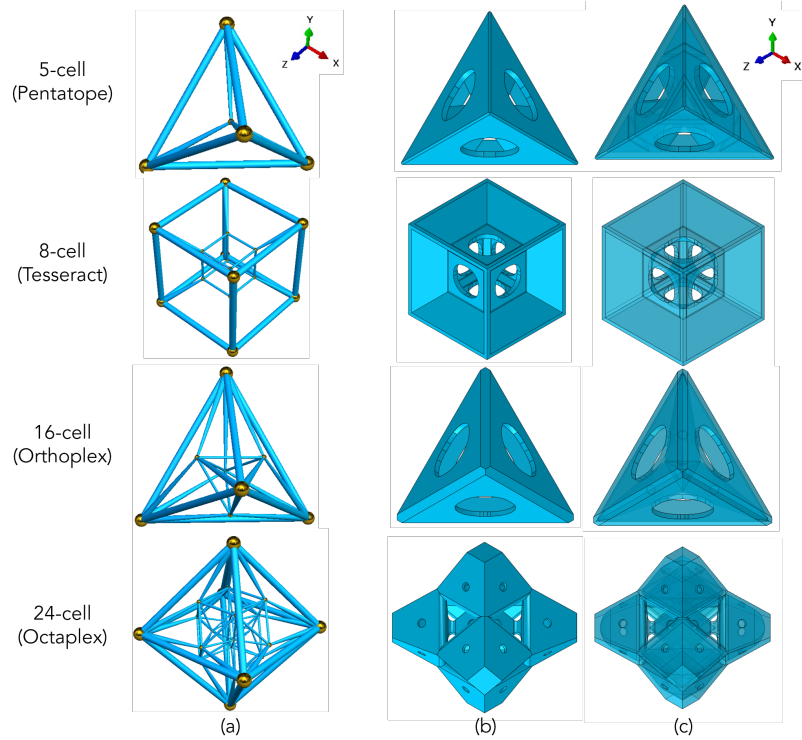


Figure 6: Regular convex 4-polytopes presented as wire-frame Schlegel diagrams (a) and the metamaterial samples based on the wireframes as solid (b) and semi-transparent (c) unit cell models.

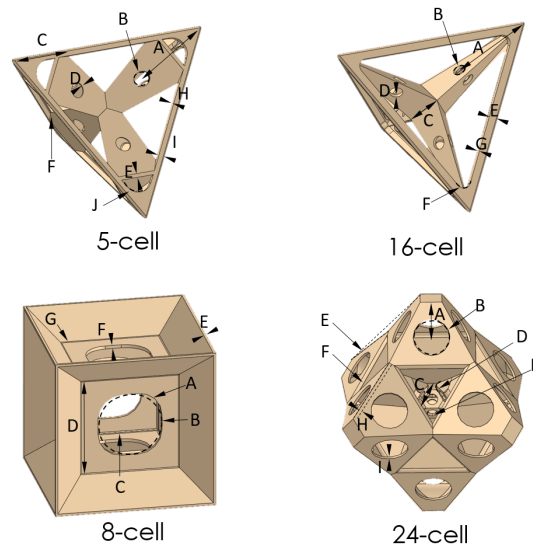


Figure 7: Parametric design approach to 3D projected 4-polytope metamaterial design. Adjustable parameters are marked in letters for each structure.

unit cell was set as an encastre boundary condition and the top was prescribed a tensile displacement at an equivalent tensile strain of 0.04. To represent the effect of neighbouring unit cells deforming in the same manner, another set of symmetry boundary conditions was used at the outer surfaces (parallel to the X and Z planes) of the quarter unit cells.

Table 5: Parametric design variables for 5, 8, 16 and 24-cell designs as illustrated in Figure 7, adapted from [34].

5-cell	8-cell	16-cell	24-cell
A Drain hole distance	A Drain hole round radius	A Drain hole distance	A Drain hole distance
B Drain hole radius	B Drain hole radius	B Drain hole radius	B Drain hole radius
C Coner distance	C Inner egde round radius	C Inner triangle size	C Inner triangle size
D Inner wall thickness	D Inner cube size	D Inner wall thickness	D Inner triangle round
E Corner wall thickness	E Outer wall thickness	E Outer shell width	E Projection angle
F Outer corner round	F Inner cube wall thickness	F Outer shell round	F Outer shell round
G Inner triangle size	G Outer egde round radius	G Outer shell width	G Inner wall thickness
H Outer shell thickness			H Middle wall thickness
I Outer shell width			I Outer wall thickness
J Outer shell round			

The structures were discretized using a free (unstructured) meshing technique as it was found to be more reliable for auto-generated structures rather than swept and structured meshes. Tetrahedral meshing elements (C3D10) were used and the mesh density was chosen following a mesh convergence (performed for each of the four 3D projected 4-polytope structures). A mesh growth rate of 1.05 was selected to discretise the features using evenly sized elements. Additionally, remeshing introduced to address any meshing difficulties arising due to the automated generation of the 3D projected 4-polytope structures during the optimization stage. The edges of each structure were seeded to maintain a minimum constraint of three elements across the thinnest feature while the element number was set to increase with increasing feature size. Such an approach was found to be effective in evaluating the through-thickness response of the thin-walled structures while maintaining an optimal mesh size that would not compromise computational results. The implicit solver utilized the Newton-Raphson method and was chosen as it enabled the use of variable size time increments without affecting the solution accuracy, therefore reducing the overall computational time when compared to the explicit solver.

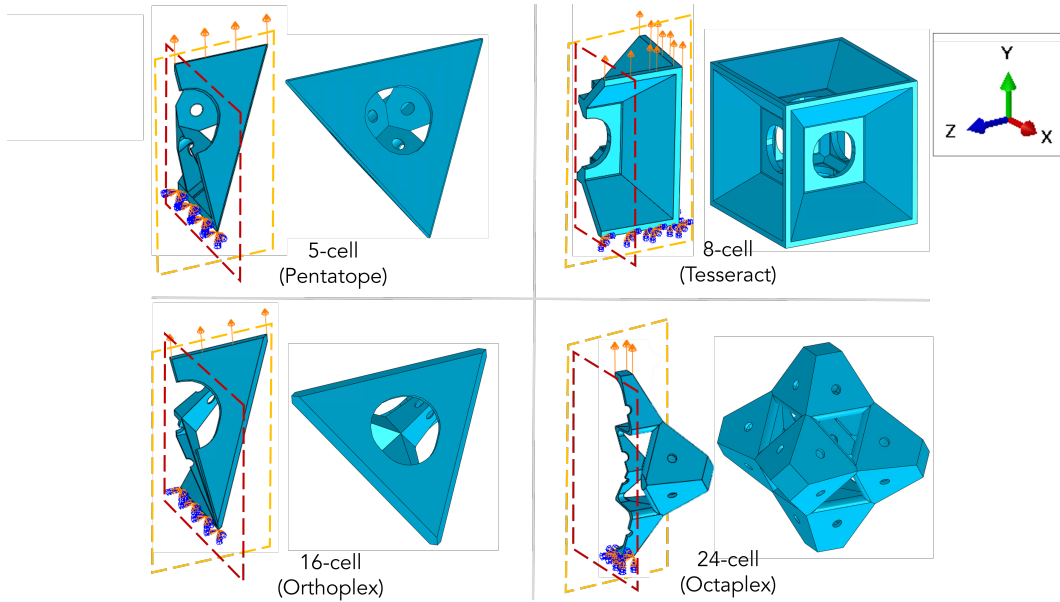


Figure 8: Summary of the boundary conditions applied to 3D projected 4-polytope metamaterial quarter unit cell models (left side) and the full unit cell illustrations (right side). The outer surfaces of each model were prescribed symmetry boundary conditions about the X and Z planes located at the interface between the neighbouring cells. Orange and red dashed lines on the quarter models (left side) mark the inner X and Z symmetry planes within the unit cells respectively which were prescribed symmetry boundary conditions. An encastre BC was used at the bottom and tensile displacement BC resulting in 0.04 strain was applied to the top of each quarter model.

The 3D projected 4-polytope geometries could be modified in an automated manner by parametrically manipulating the variables mentioned in Table 5. This therefore enabled further exploration of the design space by means of an optimization algorithm. To explore this space in an efficient manner, manufacturing constraints were incorporated which were namely: (1) minimum wall thickness and (2) minimum drain hole size. The former is limited by the peel-off force required to remove the sample from the resin tank after a new layer is 3D printed, while the latter is constrained by the viscosity of the resin and is required to ensure acceptable drainage of the hollow chambers within the 3D printed structure. Additionally, the design variable arrangements resulting in suction cups, concave features increasing the peel-off force and causing the prints to fail, were also omitted from the computational analysis. Individual steps involved in producing tensile 4-polytope samples and the overall manufacturing approach are further discussed in Section 5.3.

The 4-polytope-based meta-structures, namely the 5, 8, 16 and 24-cell, were optimized to achieve the highest specific stiffness value $\frac{E}{\rho}$, where E is Young's modulus of the unit cell in tension and ρ is the apparent density of the unit cell. This was possible through the combination of a finite element (FE) model of a unit cell, previously described in this section, with a parametric design optimization framework powered by a genetic algorithm (GA). Within this framework, parametric design variables served as the inputs to the unit cell simulations while the outputs obtained from the FE analyses were fed to the optimization algorithm to enable exploration of the design space. When launched, the genetic algorithm generated a set of inputs that were predicted to favor the objective function and used simulation outputs such as the strain energy (U) and the total mass (m) of the generated unit cell as the indicators of success. This was repeated multiple times with different inputs until the structure with the highest specific stiffness was generated. The function describing this objective in the simplest form is shown as Equation 1, where σ is the 1st Piola-Kirchhoff stress, V is the total volume of the unit cell and U_e is the total elastic strain energy. A single objective genetic algorithm was used instead of brute force methods to perform informed predictions of favorable input parameters based on stored outputs from preceding simulations. The objective function defining the specific stiffness was calculated using the elastic strain energy output (U_e) obtained from a single unit cell simulation. This is shown in full in Equation 2, where V_e is the volume of a mesh element, n is the total number of mesh elements while σ_{ij} and ϵ_{ij} are the stress tensor and the elastic strain tensor of a mesh element respectively. This procedure is run iteratively to evaluate a wide range of metamaterials and correlate individual design parameters to their effect on the final specific stiffness ($\frac{E}{\rho}$) of the structure. The algorithm then uses this information to select the best performing structures in tension and uses crossover and mutation operations to generate a new population of structures. This execution loop is run until one of the stopping conditions is met and a near-optimum design solution is generated with the highest specific stiffness ($\frac{E}{\rho}$) as compared with all structures evaluated in the simulation. A genetic algorithm flow diagram is shown in Figure 9.

$$\frac{E}{\rho} = \left(\frac{\sigma^2 V}{2U_e} \right) \left(\frac{m}{V} \right)^{-1} \quad (1)$$

$$U_e = \sum_{e=1}^n V_e \cdot \int_0^{\epsilon_{ij}} \sigma_{ij} d\epsilon_{ij} \quad (2)$$

The parameters chosen for setting up the genetic algorithm and used in the optimization framework are summarized in Table 6. The computational complexity of the problem, the availability of parallel computing power and the number of 4-polytope parametric design variables (genes in GA) were taken into account to choose a population size of 28. In order to cap the maximum optimization cycle running time, the absolute number of generations was chosen as 50. Additionally, if a better solution was not found in the last 20% of the total generations executed, the cycle was stopped to save computational time. Crossover and mutation probabilities were chosen as 0.9 and $1/q$ respectively, where q is the number of parametric design variables in the metamaterial design. Crossover and mutation distribution indexes were set to 10 and 20, respectively. The algorithm parameters were chosen to suit the generic optimization problem based on [42] and therefore parameter tuning was carried out as it is considered beyond the scope of this publication.

5.3. Manufacturing

The experimental samples were manufactured using LFS (low-force-stereolithography) 3D printers from Formlabs. A photoreactive thermosetting Clear V4 resin was used to manufacture the tensile samples using the arrays of

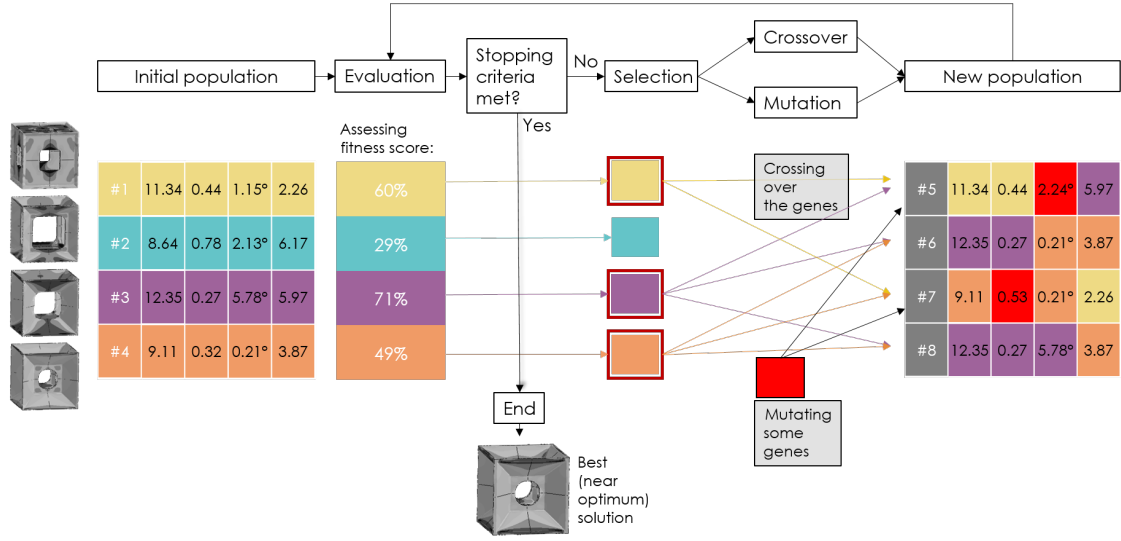


Figure 9: Schematic representation of genetic algorithm used in the optimization framework.

Table 6: Summary of the parameters used in genetic algorithm set-up, adapted from [34].

GA parameters:	
Population size	28
Abs. no. of generations	50
Crossover probability	0.9
Mutation probability*	1/q
Crossover distribution index	10
Mutation distribution index	20
Stopping criteria	no improvement in last 20% of gen.

*q is the number of parametric design variables (genes)

the unit cells previously discussed in Section 5.1. The cells were stacked to create a systematic array of $2 \times 2 \times 4$ with 16 unit cells in total and external sample dimensions of $30 \times 30 \times 120$ mm. As shown in Figure 10, the unit cells in the middle section of the tensile sample (“test unit cells”) are representative of the 3D projected 4-polytope geometries designed using the optimization framework, while the cells adjacent to the middle section (“transition structure”) have artificially higher wall thicknesses in comparison to the central unit cells. The ends of the sample were further reinforced by filling in the cavities with a two-part epoxy (RS Epoxy 406-9592) to ensure that the strength of the “gripping area” is sufficient to withstand the grip forces applied by the tensile testing machine. Such a design approach with three different areas within each tensile sample was chosen to mimic the “dog bone” geometry of tensile coupons and hence maximize the chances of failure occurring within the central part of the specimen. The 3D printer layer height was set to $25\mu\text{m}$. Following the manufacturing process, the samples were washed with isopropyl alcohol in a Form Wash, to ensure the removal of as much excess resin as possible prior to post-curing of the samples (30min at 60°C in a Form Cure UV chamber). As suggested by the manufacturer, the samples were post-cured to increase cross-linking within the polymer and hence increase the material quality of the 3D printed samples. All of the manufactured samples were found to have high dimensional accuracy with deviation between the CAD models and the experimental samples being recorded at less than 0.42%. The weight variation, Δw , was found to be 0.1162, 0.0095, 0.1267, 0.1180 for 5, 8, 16 and 24-cell, respectively and was calculated as $\Delta w = \left(\frac{w_{\text{sample}}}{w_{\text{CAD}}} - 1 \right)$, where w_{sample} is the weight of the 3D printed sampled and w_{CAD} is the weight calculated using the volume of the CAD models and the density of the cured Clear V4 resin. The main reason for variations in the sample weight when compared to the CAD models was found to be due to leftover uncured or partially-cured resin within the samples. As the internal geometry of the unit cells is highly

complex and the majority of the features are relatively small, some of the resin is inaccessible and cannot be removed during the washing stage. As such, this residual resin cures, fully or partially, during the post-curing stage. To minimize the extent of residual resin without affecting the mechanical properties of the samples, the washing procedure was adjusted for each specimen type.

In addition to the metamaterial samples, sets of gyroid and hexagonal honeycomb tensile samples were manufactured in an identical manner to carry out an experimental comparison of the mechanical properties of these more common structures against the 3D projected 4-polytope structures. A sinusoidal wave with an amplitude of 3.75 mm and a period of 30 mm was used for the gyroid structure, while the wall thickness was chosen as 0.85 mm. The apparent density of the “test unit cells” within the gyroid tensile sample is 108.82 kg/m^3 while the relative density is 9.34%. The honeycomb tensile samples were made using hexagonal unit cells with a diameter of 8.5mm and a wall thickness of 0.55mm which resulted in “test unit cells” with apparent and relative densities of 192.89 kg/m^3 and 16.56%, respectively. The hexagonal geometry was aligned so that the out-of-plane direction of the cells is in line with the tensile loading direction, in order to obtain out-of-plane properties of the honeycomb sample. Both, the gyroid and the hexagonal honeycomb tensile samples, were designed to have dedicated testing, transition and gripping areas as shown for the 4-polytope metamaterial samples in Figure 10. Representative tensile specimens of all of the 3D printed metamaterial structures, gyroid structures and hexagonal honeycomb structures are shown in Figure 11.

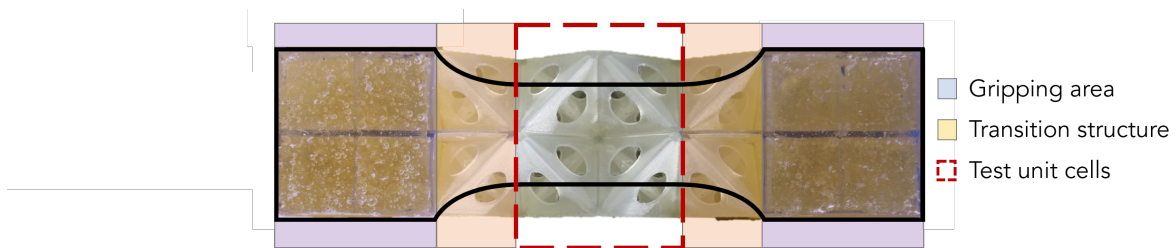


Figure 10: Tensile specimen geometry designed to recreate the tensile behaviour of a “dog bone” shape coupon (black solid line). Main specimen areas: gripping (in purple), transition structure (in orange) and dedicated test unit cells (red dashed line).

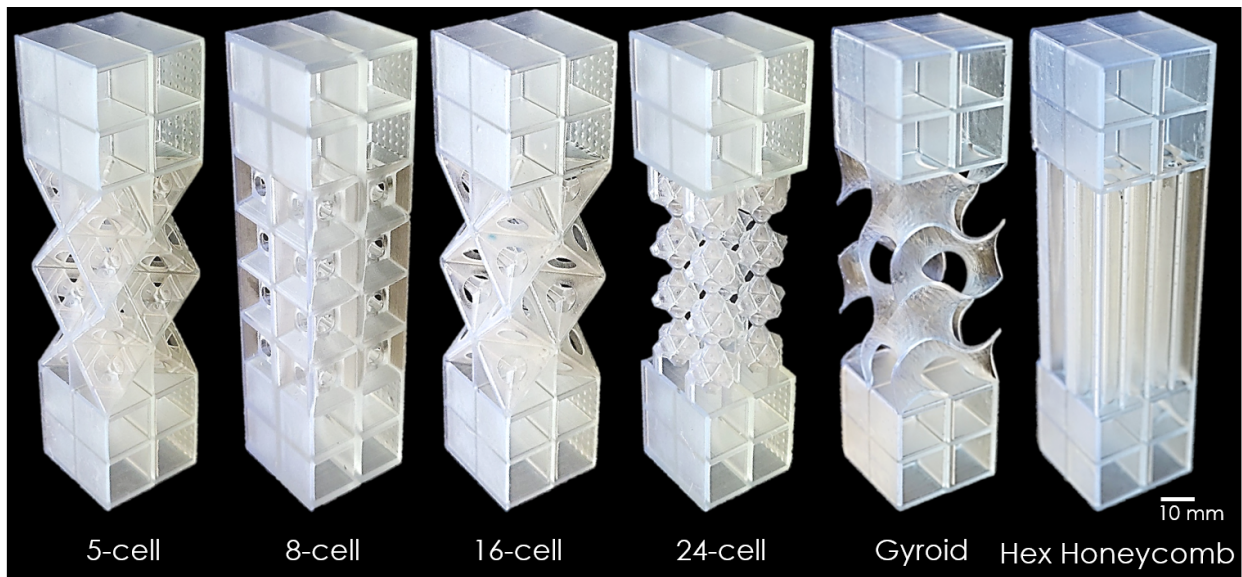


Figure 11: Representative tensile test specimens with a $2 \times 2 \times 4$ 3D projected 4-polytope unit cell array. From left to right: 5-cell, 8-cell, 16-cell and 24-cell, and additional structures used as ‘comparative experimental controls’ - gyroid and hexagonal honeycomb (tested in the out-of-plane direction).

5.4. Mechanical testing procedure

An Instron 8802 servo-hydraulic test machine mounted with a 250kN load cell and tensile grips for samples up to 32mm in diameter was used for testing specimens in tension. An Imetrum DIC system (resolution of 1400×1000 at 17.8fps) was used for taking vertical and horizontal strain measurements across the four outermost faces of the unit cells situated in the middle of the tensile specimen. This 2D image correlation technique allowed multiple measurements to be taken in both axial and transverse, directions, which were then averaged to obtain the final strain measurement values. Five specimens of each 3D projected 4-polytope metamaterial, gyroid and honeycomb structure, manufactured in the same manner, were tested in tension at a ramp rate of 10mm/min to obtain experimental results. This ramp rate was chosen to ensure Hookean behavior of the cured resin under tensile deformation.

References

- [1] S. M. Montgomery, X. Kuang, C. D. Armstrong, H. J. Qi, Recent advances in additive manufacturing of active mechanical metamaterials, *Current Opinion in Solid State and Materials Science* 24 (5) (2020) 100869. doi:10.1016/J.COSSMS.2020.100869.
- [2] J. Qi, Z. Chen, P. Jiang, W. Hu, Y. Wang, Z. Zhao, X. Cao, S. Zhang, R. Tao, Y. Li, D. Fang, Recent Progress in Active Mechanical Metamaterials and Construction Principles, *Advanced Science* 9 (1) (2022) 2102662. doi:10.1002/ADVS.202102662.
URL <https://onlinelibrary.wiley.com/doi/full/10.1002/advs.202102662><https://onlinelibrary.wiley.com/doi/abs/10.1002/advs.202102662>
- [3] M. Balan P. J. Mertens A, M. V. Bahubalendruni, Auxetic mechanical metamaterials and their futuristic developments: A state-of-art review, *Materials Today Communications* 34 (2023) 105285. doi:10.1016/J.MTCOMM.2022.105285.
- [4] T. R. Giri, R. Mailen, Controlled snapping sequence and energy absorption in multistable mechanical metamaterial cylinders, *International Journal of Mechanical Sciences* 204 (2021) 106541. doi:10.1016/J.IJMECSCI.2021.106541.
- [5] M. J. Mirzaali, H. Pahlavani, A. A. Zadpoor, Auxeticity and stiffness of random networks: Lessons for the rational design of 3D printed mechanical metamaterials, *Applied Physics Letters* 115 (2) (2019) 021901. doi:10.1063/1.5096590.
URL <https://aip.scitation.org/doi/abs/10.1063/1.5096590>
- [6] A. Rafsanjani, D. Pasini, Bistable auxetic mechanical metamaterials inspired by ancient geometric motifs, *Extreme Mechanics Letters* 9 (2016) 291–296. doi:10.1016/J.EML.2016.09.001.
- [7] X. Zheng, T. T. Chen, X. Guo, S. Samitsu, I. Watanabe, Controllable inverse design of auxetic metamaterials using deep learning, *Materials & Design* 211 (2021) 110178. doi:10.1016/J.MATDES.2021.110178.
- [8] H. Zhang, P. Chen, G. Lin, W. Sun, A corrugated gradient mechanical metamaterial: Lightweight, tunable auxeticity and enhanced specific energy absorption, *Thin-Walled Structures* 176 (2022) 109355. doi:10.1016/J.TWS.2022.109355.
- [9] Z. Zhai, Y. Wang, H. Jiang, Origami-inspired, on-demand deployable and collapsible mechanical metamaterials with tunable stiffness, *Proceedings of the National Academy of Sciences of the United States of America* 115 (9) (2018) 2032–2037. doi:10.1073/PNAS.1720171115/SUPPL_{_}FILE/PNAS.1720171115.SM04.MOV.
URL <https://www.pnas.org/doi/abs/10.1073/pnas.1720171115>
- [10] R. M. Neville, F. Scarpa, A. Pirrera, Shape morphing Kirigami mechanical metamaterials, *Scientific Reports* 2016 6:1 6 (1) (2016) 1–12. doi:10.1038/srep31067.
URL <https://www.nature.com/articles/srep31067>
- [11] Z. Zhai, L. Wu, H. Jiang, Mechanical metamaterials based on origami and kirigami, *Appl. Phys. Rev* 8 (2021) 41319. doi:10.1063/5.0051088.
URL <https://doi.org/10.1063/5.0051088>
- [12] X. Yu, J. Zhou, H. Liang, Z. Jiang, L. Wu, Mechanical metamaterials associated with stiffness, rigidity and compressibility: A brief review, *Progress in Materials Science* 94 (2018) 114–173. doi:10.1016/J.PMATSCI.2017.12.003.
- [13] J. Hu, A. T. Tan, H. Chen, X. Hu, Superior compressive properties of 3D printed plate lattice mechanical metamaterials, *International Journal of Mechanical Sciences* 231 (2022) 107586. doi:10.1016/J.IJMECSCI.2022.107586.
- [14] X. Zheng, H. Lee, T. H. Weisgraber, M. Shusteff, J. DeOtte, E. B. Duoss, J. D. Kuntz, M. M. Biener, Q. Ge, J. A. Jackson, S. O. Kucheyev, N. X. Fang, C. M. Spadaccini, Ultralight, ultrastiff mechanical metamaterials, *Science* 344 (6190) (2014) 1373–1377. doi:10.1126/SCIENCE.1252291/SUPPL_{_}FILE/ZHENG.SM.PDF.
URL <https://www.science.org/doi/10.1126/science.1252291>
- [15] M. Bessa, P. Glowacki, M. Houlder, Bayesian Machine Learning in Metamaterial Design: Fragile Becomes Supercompressible, *Advanced Materials* 31 (48) (2019). doi:10.1002/adma.201904845.
- [16] N. Yang, Y. Deng, S. Zhao, Y. Song, J. Huang, N. Wu, Mechanical Metamaterials with Discontinuous and Tension/Compression-Dependent Positive/Negative Poisson's Ratio, *Advanced Engineering Materials* 24 (3) (2022) 2100787. doi:10.1002/ADEM.202100787.
URL <https://onlinelibrary.wiley.com/doi/full/10.1002/adem.202100787><https://onlinelibrary.wiley.com/doi/abs/10.1002/adem.202100787>
- [17] T. C. Lim, Composite microstructures with Poisson's ratio sign switching upon stress reversal, *Composite Structures* 209 (2019) 34–44. doi:10.1016/J.COMPSTRUCT.2018.10.074.
- [18] H. Wu, R. Zhong, W. Chen, M. Fu, A novel mechanical metamaterial with dramatically different elastic parameters in tension and compression, *Materials Today Communications* 34 (2023) 105385. doi:10.1016/J.MTCOMM.2023.105385.
- [19] M. Chen, M. Fu, L. Hu, Poisson's ratio sign-switching metamaterial with stiffness matrix asymmetry and different elastic moduli under tension and compression, *Composite Structures* 275 (2021) 114442. doi:10.1016/J.COMPSTRUCT.2021.114442.
- [20] A. Rafsanjani, A. Akbarzadeh, D. Pasini, A. Rafsanjani, A. Akbarzadeh, D. Pasini, Snapping Mechanical Metamaterials under Tension, *Advanced Materials* 27 (39) (2015) 5931–5935. doi:10.1002/ADMA.201502809.
URL <https://onlinelibrary.wiley.com/doi/full/10.1002/adma.201502809><https://onlinelibrary.wiley.com/doi/abs/10.1002/adma.201502809>
- [21] H. Yang, L. Ma, Multi-stable mechanical metamaterials with shape-reconfiguration and zero Poisson's ratio, *Materials & Design* 152 (2018) 181–190. doi:10.1016/J.MATDES.2018.04.064.
- [22] Y. Zhang, Y. Wang, C. Q. Chen, Ordered deformation localization in cellular mechanical metamaterials, *Journal of the Mechanics and Physics of Solids* 123 (2019) 28–40. doi:10.1016/J.JMPS.2018.08.025.
- [23] M. J. Khoshgoftar, A. Barkhordari, S. Seifoori, M. J. Mirzaali, Elasticity Approach to Predict Shape Transformation of Functionally Graded Mechanical Metamaterial under Tension, *Materials* 2021, Vol. 14, Page 3452 14 (13) (2021) 3452. doi:10.3390/MA14133452.
URL <https://www.mdpi.com/1996-1944/14/13/3452/html><https://www.mdpi.com/1996-1944/14/13/3452>
- [24] Y. Jiang, Q. Wang, Highly-stretchable 3D-architected Mechanical Metamaterials, *Scientific Reports* 2016 6:1 6 (1) (2016) 1–11. doi:10.1038/srep34147.
URL <https://www.nature.com/articles/srep34147>

- [25] H. Yang, W. H. Müller, Size effects of mechanical metamaterials: a computational study based on a second-order asymptotic homogenization method, *Archive of Applied Mechanics* 91 (3) (2021) 1037–1053. doi:10.1007/s00419-020-01808-x.
URL <https://doi.org/10.1007/s00419-020-01808-x>
- [26] B. Deng, A. Zareei, X. Ding, J. C. Weaver, C. H. Rycroft, K. Bertoldi, B. Deng, A. Zareei, X. Ding, J. C. Weaver, C. H. Rycroft, K. Bertoldi, Inverse Design of Mechanical Metamaterials with Target Nonlinear Response via a Neural Accelerated Evolution Strategy, *Advanced Materials* 34 (41) (2022) 2206238. doi:10.1002/ADMA.202206238.
URL <https://onlinelibrary.wiley.com/doi/full/10.1002/adma.202206238><https://onlinelibrary.wiley.com/doi/abs/10.1002/adma.202206238><https://onlinelibrary.wiley.com/doi/10.1002/adma.202206238>
- [27] H. M. Sheikh, T. Meier, B. Blankenship, Z. Vangelatos, N. Zhao, P. S. Marcus, C. P. Grigoropoulos, Systematic design of Cauchy symmetric structures through Bayesian optimization, *International Journal of Mechanical Sciences* (2022) 107741 doi:10.1016/J.IJMECSCI.2022.107741.
- [28] Y. Wang, Q. Zeng, J. Wang, Y. Li, D. Fang, Inverse design of shell-based mechanical metamaterial with customized loading curves based on machine learning and genetic algorithm, *Computer Methods in Applied Mechanics and Engineering* 401 (2022) 115571. doi:10.1016/J.CMA.2022.115571.
- [29] L. Wang, H.-T. Liu, Parameter optimization of bidirectional re-entrant auxetic honeycomb metamaterial based on genetic algorithm, *Composite Structures* 267 (2021). doi:10.1016/j.compstruct.2021.113915.
- [30] R.-B. Yang, J. Yang, S. Lo, Wideband square spiral metamaterial absorbers based on flaky carbonyl iron/epoxy composites, *AIP Advances* 10 (1) (2020). doi:10.1063/1.5130470.
- [31] L. Singleton, J. Cheer, S. Daley, Design of a resonator-based metamaterial for broadband control of transverse cable vibration, in: *Proceedings of the International Congress on Acoustics*, Vol. 2019-September, International Commission for Acoustics (ICA), 2019, pp. 5589–5596. doi:10.18154/RWTH-CONV-239432.
- [32] M. Mansouree, A. Arbabi, Metasurface Design Using Level-Set and Gradient Descent Optimization Techniques, in: *2019 International Applied Computational Electromagnetics Society Symposium in Miami, ACES-Miami 2019*, Institute of Electrical and Electronics Engineers Inc., 2019.
- [33] H. Pahlavani, M. Amani, M. C. Saldívar, J. Zhou, M. J. Mirzaali, A. A. Zadpoor, Deep learning for the rare-event rational design of 3D printed multi-material mechanical metamaterials, *Communications Materials* 2022 3:1 3 (1) (2022) 1–11. doi:10.1038/s43246-022-00270-2.
URL <https://www.nature.com/articles/s43246-022-00270-2>
- [34] G. Cerniauskas, P. Alam, Compressive properties of parametrically optimised mechanical metamaterials based on 3D projections of 4D geometries — *Engineering Archive*.
URL <https://engrxiv.org/preprint/view/2796/version/4009>
- [35] Z. Yang, P. Alam, Designing Hierarchical Honeycombs to Mimic the Mechanical Behaviour of Composites, *Journal of Composites Science* 2021, Vol. 5, Page 17 5 (1) (2021) 17. doi:10.3390/JCS5010017.
URL <https://www.mdpi.com/2504-477X/5/1/17/html><https://www.mdpi.com/2504-477X/5/1/17>
- [36] C. C. Vu, T. T. N. Truong, J. Kim, Fractal structures in flexible electronic devices, *Materials Today Physics* 27 (2022) 100795. doi:10.1016/J.MTPHYS.2022.100795.
- [37] R. S. Farr, Y. Mao, Fractal space frames and metamaterials for high mechanical efficiency, *EPL* 84 (2008) 14001. doi:10.1209/0295-5075/84/14001.
URL www.epljournal.org
- [38] D. Wang, L. Dong, G. Gu, D. Wang, L. Dong, G. Gu, 3D Printed Fractal Metamaterials with Tunable Mechanical Properties and Shape Reconfiguration, *Advanced Functional Materials* (2022) 2208849 doi:10.1002/ADFM.202208849.
URL <https://onlinelibrary.wiley.com/doi/full/10.1002/adfm.202208849><https://onlinelibrary.wiley.com/doi/abs/10.1002/adfm.202208849><https://onlinelibrary.wiley.com/doi/10.1002/adfm.202208849>
- [39] D. Rayneau-Kirkhope, Y. Mao, R. Farr, Ultralight fractal structures from hollow tubes, *Physical Review Letters* 109 (20) (2012) 204301. doi:10.1103/PHYSREVLETT.109.204301/FIGURES/4/MEDIUM.
URL <https://journals.aps.org/prl/abstract/10.1103/PhysRevLett.109.204301>
- [40] H. Yang, B. E. Abali, D. Timofeev, W. H. Müller, Determination of metamaterial parameters by means of a homogenization approach based on asymptotic analysis, *Continuum Mechanics and Thermodynamics* 32 (5) (2020) 1251–1270. doi:10.1007/s00161-019-00837-4.
- [41] J. Bauer, L. R. Meza, T. A. Schaedler, R. Schwaiger, X. Zheng, L. Valdevit, Nanolattices: An Emerging Class of Mechanical Metamaterials, *Advanced Materials* 29 (2017) 1701850. doi:10.1002/adma.201701850.
URL <https://onlinelibrary.wiley.com/doi/10.1002/adma.201701850>
- [42] S. Katoch, S. S. Chauhan, V. Kumar, A review on genetic algorithm: past, present, and future, *Multimedia Tools and Applications* 80 (5) (2021) 8091–8126. doi:10.1007/S11042-020-10139-6/FIGURES/8.
URL <https://link.springer.com/article/10.1007/s11042-020-10139-6>